A&A 522, A61 (2010)
DOI: 10.1051/0004-6361/201015036

Astronomy & Astrophysics

3D MHD simulations of magnetic field evolution and radio polarization of barred galaxies

B. Kulesza-Żydzik, K. Kulpa-Dybeł, K. Otmianowska-Mazur, M. Soida, and M. Urbanik

Astronomical Observatory, Jagiellonian University, ul Orla 171, 30-244 Kraków, Poland
e-mail: kulesza@oa.uj.edu.pl

Received 25 May 2010 / Accepted 23 June 2010

ABSTRACT

Aims. We study numerically the large-scale gas and magnetic field evolution of barred galaxies in the gravitational potential of a disk, bulge, halo, and bar. We solve non-linear MHD equations including the back-reaction of the magnetic field to the gas. We do not take into account any dynamo process.
Methods. We apply the numerical MHD code to calculate the model of the galaxy in three dimensions. We construct realistic maps of high-frequency (Faraday rotation free) polarized radio emission on the basis of the simulated magnetic fields. The polarization model includes the effects of projection and limited resolution.
Results. The main result is that our modeled polarization maps resemble the radio polarization structures observed in barred galaxies. The modeled polarization $\boldsymbol{B}$-vectors distribution along the bar and between spiral arms resembles the observed topology of the magnetic field in barred galaxies. Our calculations for several different rotational velocities and sound speeds give the same result we got in our previous earlier published model. The reason of this behaviour is the dynamical evolution of the bar that causes gas to form spiral waves going radially outward. A gaseous spiral arms in turn generates magnetic ones, which live much longer in the inter-arm disk space than the gaseous pattern.

Key words. magnetohydrodynamics (MHD) – methods: numerical – galaxies: ISM – galaxies: magnetic fields

1. Introduction

The main reason that people are interested in studies of barred galaxies is that bars are very often observed among spiral galaxies. In the sample of 186 bright galaxies Eskridge et al. (2002) found that 56% of them were strongly, and 16% were weakly barred as observed in the H band. The next survey of 53 spiral galaxies analyzed in the K band by Grosbol (2002) showed that even 75% of spirals posses bars. There are many morphological and dynamical classes of bars. The bar shape can be very different: from rectangular to elliptical forms with short, medium, or long sizes (Athanassoula 2005a). Their speed of rotation can also be fast or slow. The form of the accompanying bulges can be classical (spheroidal shape), boxy/peanut, or disky ones (Athanassoula 2009). All these observations about bars, starting from their origin, evolution, and morphology should be explained by a physical theory. The N-body simulations of the mical development of barred galaxies show that bars are created naturally from the galactic disk (see Athanassoula 2009, and references therein). This process strongly depends on the halo-to-disk mass ratio, and on the velocity dispersion of stars in the disk (Athanassoula 2005b; Binney & Tremaine 2008). A faster growth is observed in more massive and cooler (i.e. showing lower velocity dispersion) disks. The appearance of the bar causes the redistribution of the angular momentum and its outward transport. It results in a decreasing of the pattern speed of the bar (Athanassoula 2009).

We will discuss our results of 3D numerical MHD simulations in the context of two papers: Athanassoula (1992), and Patsis & Athanassoula (2000). In the first one, the author made hydrodynamical numerical simulations in 2D, showing that the dynamics of gas is closely related to the configuration of orbits in the gravitational potential of the galaxy, which is influenced by the gravitational potential of the bar. The morphological features obtained in the experiment (dust lanes at leading edges of the bar, lack of the gas inside the bar region) are very similar to observed ones. The observational positions of dust lanes are identified with the shock regions obtained in the numerical model. The 2D SPH simulations presented in the second paper (Patsis & Athanassoula 2000) showed that the morphology of dust lanes were similar for two slow sound speeds (10 km s^{-1} and 15 km s^{-1}). For the experiment with the fastest sound speed (30 km s^{-1}) the structure of the dust lanes has changed, but this value of the sound speed is not found in real galaxies. The radio polarization observations of several of barred galaxies were reported in the literature (Beck et al. 1999, 2002, 2005; Harnett et al. 2004). The main features observed in galaxies with massive bars (e.g. NGC 1097 and NGC 1365, Beck et al. 2005) could be described as follows. The polarized intensity (PI) distribution forms ridges along the dust lanes at the leading edges of the bar in the inner part of the galaxy. Depolarized valleys are located upstream of the dust lanes as the result of a rapid change of the magnetic field direction within the telescope beam. The magnetic field vectors form a spiral pattern in the outer part of the disk, with the maxima of PI along the spiral gaseous arms and in the inter-arm regions (Beck et al. 2005). The magnetic field configuration in barred galaxies seems to be very complicated compared to the observed gas flows. It is not yet understood what kind of mechanisms could be responsible for this behaviour of the magnetic field in barred galaxies.

A number of works (Otmianowska-Mazur et al. 1997, 2002; Moss et al. 1998, 1999, 2001, 2007; Kulesza-Żydzik et al. 2009)

have been done to study numerically the magnetic field evolution in barred galaxies. The results of 3D numerical simulations of magnetohydrodynamic (MHD) evolution of one example, NGC 1365 (Moss et al. 2007), show that even after checking the whole range of input parameters there is no agreement between the topology of the polarization vectors observed in this galaxy and given by computations. The results of our *N*-body and MHD simulations (Otmianowska-Mazur et al. 2002) explain the mechanism responsible for detaching of the magnetic arms from the gaseuos spiral and their drift into the inter-arm regions. The gravitational potential of the bar (which consists of stars and gas) rotates faster than the matter in the disk, creating gaseous spiral arms. The magnetic field, present in the galactic disk, is influenced by gas flow in the non-axisymmetric structures and forms magnetic arms along the spiral arms and magnetic structures along the bar leading edges. The magnetic arm outside of the corotation radius drifts owing to the difference between the pattern speed of the bar (together with the gaseous arms) and the rotation speed of the disk into the inter-arm space. Each magnetic arm encounters another gaseous one and/or also joins the magnetic structure formed later. The situation repeats itself a few times during the galactic life (Otmianowska-Mazur et al. 2002). Our results of 3D non-linear MHD numerical simulations taking into account the back-reaction of magnetic field to gas (Kulesza-Żydzik et al. 2009) have shown that the same process works.

We present the results of the new calculations made under the assumption applied earlier in Kulesza-Żydzik et al. (2009), where we computed only one set of the initial parameters. Similarly, we solve the 3D MHD equations including the back-reaction of the magnetic field on the gas, using the analytically prescribed gravitational potential of the disk, halo, bulge, and bar. We apply the code constructed by Kowal et al. (2009; see also Kulesza-Żydzik et al. 2009). We check how parameters like the rotational velocity of the bar and the sound speed control the mechanism of the magnetic arm drifting from the gaseous spiral arms into the inter-arm regions.

2. Model description

2.1. Numerical methods

All calculations were performed using the Godunov code (Kowal et al. 2009) based on the essentially non-oscillatory (ENO) spatial reconstruction, Harten-Lax-van-Leer (HLL) approximate Riemann-solver, Runge-Kutta (RK) time integration (Del Zanna et al. 2003) to solve isothermal MHD equations, and constrained transport method (Evans & Hawley 1988) to keep a zero magnetic field divergence. The computational domain covers 30 kpc × 30 kpc × 7.5 kpc of space with 512×512×128 cells of a 3D cartesian grid, which yields about 60 pc of spatial resolution in each direction.

2.2. Basic equations

We investigate the evolution of a barred galaxy by solving the set of MHD equations:

$$\frac{\partial \rho}{\partial t} + \nabla \cdot (\rho \boldsymbol{v}) = 0, \tag{1}$$

$$\frac{\partial \boldsymbol{v}}{\partial t} + (\boldsymbol{v} \cdot \nabla)\, \boldsymbol{v} = -\frac{1}{\rho}\nabla p - \nabla \Phi - \frac{1}{4\pi\rho}\,(\nabla \times \boldsymbol{B}) \times \boldsymbol{B}, \tag{2}$$

$$\frac{\partial \boldsymbol{B}}{\partial t} = \nabla \times (\boldsymbol{v} \times \boldsymbol{B} - \eta \nabla \times \boldsymbol{B})\,, \tag{3}$$

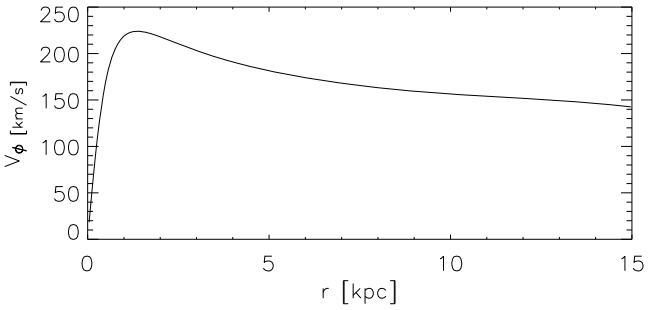

Fig. 1. Rotation curve of the gas in the galactic midplane at the beginning of simulations ($t = 0$).

$$\nabla \cdot \boldsymbol{B} = 0, \tag{4}$$

where $\boldsymbol{v}$ is the large-scale gas velocity field, ρ is the gas density, p is the gas pressure, Φ is the gravitational potential, $\boldsymbol{B}$ is the magnetic induction and η is the turbulent magnetic diffusivity. To make this set of equations complete we add an isothermal equation of state:

$$p = \rho c_{\rm s}^2, \tag{5}$$

where $c_{\rm s}$ is the constant, isothermal sound speed.

2.3. The initial conditions and input parameters

Our model of the galaxy consists of four components: the large massive halo, the central bulge, the rotating disk of stars, and the bar. They are represented by different analytical gravitational potentials.

The stellar disk is represented by the isochrone gravitational potential (Binney & Tremaine 2008) of the form

$$\Phi_{\rm d} = -\frac{GM_{\rm d}}{a_{\rm d} + \sqrt{a_{\rm d}^2 + r^2}}, \tag{6}$$

where $M_{\rm d}$ is the disk total mass, $a_{\rm d}$ is its characteristic scale length, and r is the distance to the galactic center in cylindrical coordinates (r, ϕ, z). The gravitational potentials of the halo and the bulge components are described by two Plummer spheres:

$$\Phi_{\rm b,h} = -\frac{GM_{\rm b,h}}{\sqrt{z^2 + r^2 + a_{\rm b,h}^2}}, \tag{7}$$

where b, h stands for the bulge and the halo respectively, $M_{\rm b,h}$ is the mass of each component and $a_{\rm b,h}$ is responsible for the scale length of the bulge and the halo. The rotation curve of the gas generated by a sum of these gravitational potentials is presented in Fig. 1.

The bar component is described by the second order Ferrers ellipsoid with semi-axes (a, b, b). It is introduced into the galaxy gradually in time, until it reaches its final mass $M_{\rm bar}$ (from t = 0.1 Gyr to t = 0.4 Gyr). In order to conserve the total mass of the galaxy we reduce the bulge mass, so we have $M_{\rm bar}(t) + M_{\rm b}(t)$ = const. during the calculations. The bar rotates with a constant angular speed $\Omega_{\rm bar}$.

We assume that the initial gas distribution has the general form

$$\rho(z, r) = \rho_0 P(z, r) Q(r), \tag{8}$$

Table 1. Values of the input parameters.

Parameter	Value	
M_d	4.0×10^{10}	$M_\odot$
a_d	0.6	kpc
$M_{\mathrm{b},t=0}$	1.5×10^{10}	$M_\odot$
a_b	5.0	kpc
M_h	1.2×10^{11}	$M_\odot$
a_h	15.0	kpc
M_bar	1.5×10^{10}	$M_\odot$
a	6.0	kpc
b	3.0	kpc
Ω_bar	$15.0 \div 50.0$	Gyr^{-1}
ρ_0	1.0	$H\ \mathrm{cm}^{-3}$
c_s	$5.0 \div 10.0$	$\mathrm{km\ s}^{-1}$
R	13.5	kpc
α	10.0	
β	10^3	
$B_{\varphi,t=0}$	0.144	μG
η	3.017×10^{25}	$\mathrm{cm}^2\ \mathrm{s}^{-1}$

where ρ_0 means gas density at the galactic center. Solving the equation of motion (2) in z direction one can get

$$P(z,r) = \exp\left\{\frac{\beta G}{c_\mathrm{s}^2(1+\beta)}\left(\frac{M_\mathrm{b}}{\sqrt{z^2+r^2+a_\mathrm{b}^2}} - \frac{M_\mathrm{b}}{\sqrt{r^2+a_\mathrm{b}^2}} + \frac{M_\mathrm{h}}{\sqrt{z^2+r^2+a_\mathrm{h}^2}} - \frac{M_\mathrm{h}}{\sqrt{r^2+a_\mathrm{h}^2}}\right)\right\}. \quad (9)$$

For numerical reasons (the problem has a rotational symmetry, while MHD equations are solved in the cartesian grid) we modified the gas density distribution by introducing a truncation factor $Q(r)$:

$$Q(r) = \frac{2}{\mathrm{e}^{(r/R)^\alpha} + \mathrm{e}^{(r/R)^{-\alpha}}}, \quad (10)$$

which strongly reduces the density for $r \gg R$. The self-gravity of the gas is not taken into account.

We assume that the initial magnetic field is purely azimuthal and its distribution strictly depends on the gas distribution through the condition

$$\beta = \frac{8\pi\rho {c_\mathrm{s}}^2}{B^2} = \mathrm{const.}, \quad (11)$$

where β measures the ratio of the thermal to the magnetic pressure of the gas at the beginning of simulations. The initial magnetic field distribution has the form

$$B_{z,t=0} = 0, \qquad B_{r,t=0} = 0, \qquad B_{\varphi,t=0} = \sqrt{\frac{8\pi\rho_{t=0}{c_\mathrm{s}}^2}{\beta}}. \quad (12)$$

The existence and the evolution of the morphological features in barred galaxies depends on a variety of input parameters. Values of the model parameters are presented in Table 1. We analyzed the influence of the bar angular velocity and the sound speed (Ω_bar, c_s) upon the gas flows and final structure of the magnetic field. Values of the bar angular velocity and the sound speed for selected models are presented in Table 2 (iILR and oILR are the positions of the two inner Lindblad resonances, OLR is the position of the outer Lindblad resonance, CR is the corotation radius where $\Omega_\mathrm{bar} = \omega(r)$, see Binney & Tremaine 2008, for more detailes).

Table 2. Positions of Lindblad resonances for selected angular speeds of the bar and sound speeds.

Model	c_s [$\mathrm{km\ s}^{-1}$]	Ω_bar [Gyr^{-1}]	iILR [kpc]	oILR [kpc]	CR [kpc]	OLR [kpc]
omb15cs07	7.0	15.0	0.24	4.64	11.39	>15.00
omb20cs07	7.0	20.0	0.29	3.73	8.29	12.58
omb25cs07	7.0	25.0	0.33	3.06	6.90	10.44
omb30cs07	7.0	30.0	0.38	2.58	5.94	8.91
omb50cs07	7.0	50.0	0.69	1.31	3.93	5.81
omb25cs05	5.0	25.0	0.33	3.06	6.90	10.44
omb25cs07	7.0	25.0	0.33	3.06	6.90	10.44
omb25cs10	10.0	25.0	0.33	3.06	6.90	10.43

Notes. All resonances are calculated for the initial rotation curve ($t = 0$).

2.4. Stokes parameters

The synthetic radio polarization maps enable us to compare our simulations directly with the observed properties of barred galaxies. To obtain the intensity and the polarization angles of $\boldsymbol{B}$-vectors as seen in the radio polarymetry, we integrate the Stokes parameters Q and U of the synchrotron emissivity along a number of lines of sight. We assume the Gaussian radial and vertical distribution of relativistic electrons. The assumed truncation radius and the height scale are equal 13.5 kpc and 3 kpc, respectively. In order to directly compare our results with real observations we convolve our calculated Q and U distributions with a Gaussian beam (of 40″ – which corresponds to 1.14 kpc) prior to combining them into maps of polarized intensity and position angle.

3. Results for the reference model

As a reference for the discussion below we chose the model calculated with $\Omega_\mathrm{bar} = 25\ \mathrm{Gyr}^{-1}$ and $c_\mathrm{s} = 7\ \mathrm{km\,s}^{-1}$ (the name *omb25cs07* will be used). The angular speed of the bar determines the corotation radius and the existence of Lindblad resonances (Binney & Tremaine 2008), so it has a major influence on the spiral arms generation. For $\Omega_\mathrm{bar} = 25\ \mathrm{Gyr}^{-1}$ we have all the resonances inside the galaxy and corotation radius outside of the bar (see Table 2). Our selection of the sound speed value is a compromise between various realistic values adopted by other authors (Patsis & Athanassoula 2000; Englmaier & Gerhard 1997; Otmianowska-Mazur & Chiba 1995) and our model numerical abilities.

3.1. Time evolution of a barred galaxy

In order to show and shortly describe the basic dynamical features of our main model, we present the gas density distribution and the velocity field for a few time steps of galactic evolution (see Fig. 2). In the galactic midplane we can observe well defined structures (spiral arms, dust lanes, central bulge), which are changing their appearance in time. The bar is gradually introduced into the galaxy in time from 0.1 Gyr to 0.4 Gyr (it takes about 1.2 rotation of the bar). At the same time two arc-like structures appears in the central part of the galaxy, inside the bar region (see Fig. 2, 0.22 Gyr), which can be identified with the gas density enhancements along the leading edges of the bar. From the time step of 0.4 Gyr the bar mass does not change, but the gas distribution in the disk still changes rapidly. Two arcs formed earlier evolve into two streams of gas along the leading

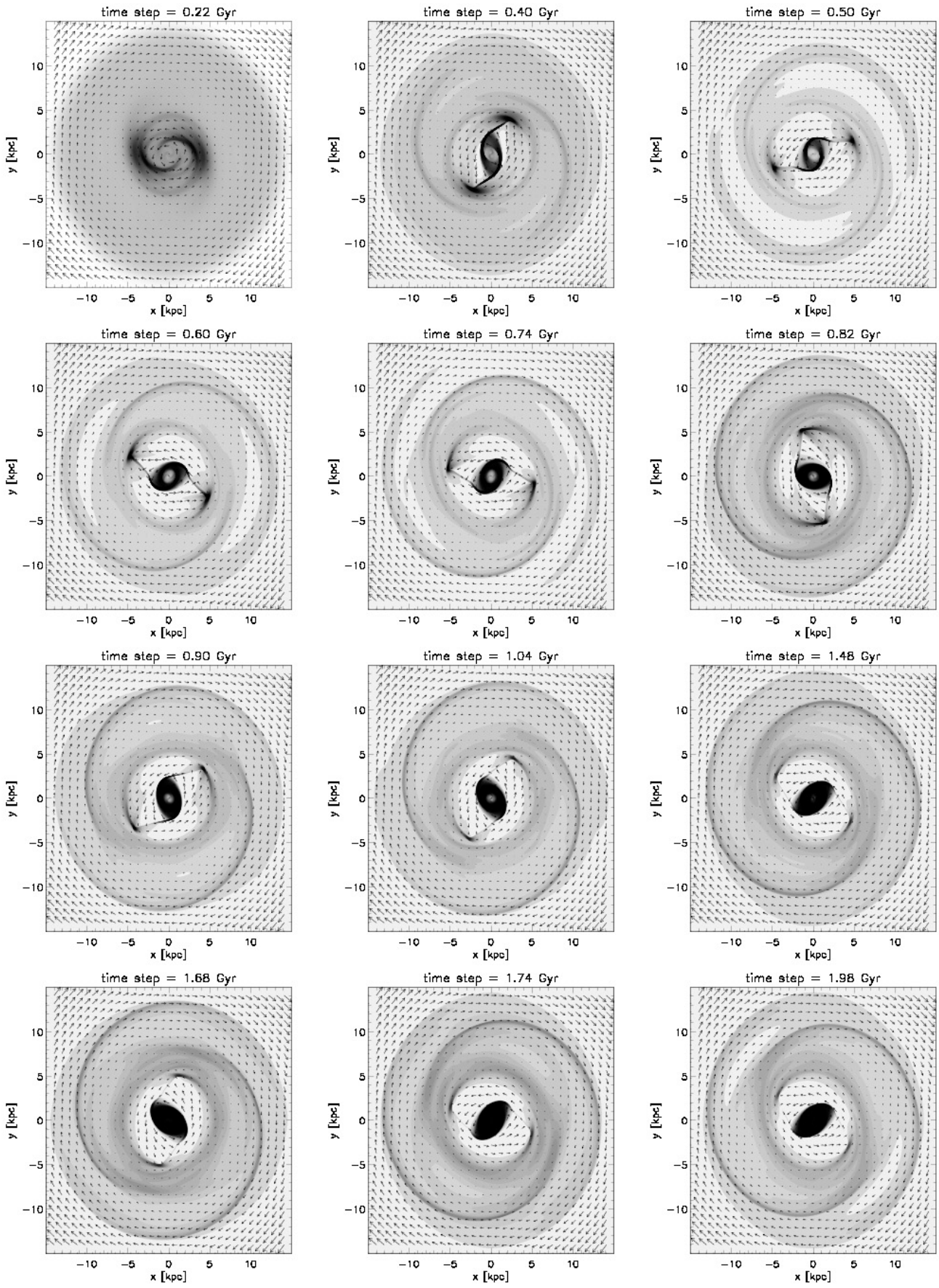

Fig. 2. Gas density distribution (grey scale) and the gas velocity field (vectors) in the galactic midplane for selected time steps (at the top of each picture) of the *omb25cs07* galaxy evolution. Both gas and the bar are rotating counter-clockwise, so the velocity field shows the gas rotation with respect to the frame of the bar.

edges of the bar, which can be identified as the dust lanes (very well defined from $t = 0.4$ Gyr to $t = 1.04$ Gyr), with strong density enhancements at their outer ends and in the galactic center. Strong changes of velocity vectors directions along these gas streams confirm the existence of strong shocks in these regions. In the outer parts of the galaxy the gas density enhancement forms two trailing spiral arms (visible from $t = 0.4$ Gyr). After about 1.0 Gyr the outer spiral arms are well defined, while the gas streams inside the bar are less visible (time steps 1.48 Gyr, 1.68 Gyr, 1.74 Gyr, 1.98 Gyr). The patterns of the velocity vectors show that shocks are still strong here. During a few rotations of the bar almost all the gas from the central part of the galaxy is transferred to the outer regions of the galactic disk ($r > 6$ kpc) or to its nucleus ($r < 3$ kpc). The strongest enhancement of the gas density in the galactic center seems to be related with the positions of the two inner Lindblad resonances (iILR = 0.33 kpc and oILR = 3.06 kpc, see Table 2).

3.2. Magnetic field structure

Figure 3 shows the magnetic field evolution as seen in radio polarymetry in time for our reference model *omb25cs07* for the same time steps as in Fig. 2. We present here the distribution of the polarization angle and the polarized intensity superimposed onto the column density during 2.00 Gyr of galactic evolution. All face-on polarization maps have been smoothed to the resolution 40″. The black color represents the regions with the highest density. At first the magnetic field maxima correspond to the gas density enhancement, which can easily be seen at the time step $t = 0.40$ Gyr. At this time step we notice two polarized magnetic arms aligned along the gaseous ones, a strong magnetic field in the central part of the galaxy and a magnetic ring which encircles the bar. No magnetic field is present in the inter-arm regions or in the area between the magnetic ring and the central part of the bar. However, at the next time step ($t = 0.50$ Gyr) the magnetic arms start to detach from the gaseous spirals and drift into the inter-arm regions (see time steps: $t = 0.60$ Gyr, $t = 0.74$ Gyr). Also the magnetic ring that encircles the bar becomes thicker, but in the area between ring and the central part of the bar we do not get the magnetic field enhancement during the whole simulation time. Finally, at time step $t = 0.82$ Gyr the magnetic arms connect with the inner magnetic ring and form a double-ring structure. This situation is not permanent, and at the time step $t = 1.04$ Gyr the double-ring structure is no longer present. What is more, at the time step $t = 1.48$ Gyr the magnetic arms are also not present in the inter-arm region and the magnetic field distribution is similar to these shown at the time step $t = 0.40$ Gyr. We estimated that the process during which the magnetic arms detach from the gaseous spiral, then connect with magnetic ring which encirles the bar and finally disappear from the inter-arm region takes approximately 1.0 Gyr, which corresponds to four rotation periods of the bar. The effect described above repeats and at the time step $t = 1.68$ Gyr magnetic arms again drift into the inter-arm region and form the double-ring structure.

The drift of the magnetic arms into the inter-arm area was described in our previous paper (Kulesza-Żydzik et al. 2009), where we concluded that this behaviour is caused by the difference in the angular velocity of the magnetic arms and the gaseous spirals. Namely, the magnetic arms do not corotate with gaseous spiral structure, but follow the general gas motion in the disk, which has a slightly lower angular velocity. However, in the previous paper the recurrence of this effect was not confirmed yet, mainly because of the simulation time, which was too short.

3.3. Magnetic pitch angles

In Fig. 4 we present our results in the frame of the azimuthal angle in the disk and $\ln(r)$ (r being the galactocentric distance). Using this coordinate system we can easily compare the pitch angles of the magnetic and gaseous arms, because the logarithmic spiral is represented by a straight line inclined by its pitch angle. In Fig. 4 we plot the contours of the polarized intensity and polarized B-vectors superimposed onto the gas density (integrated along the line of sight) for four time steps: $t = 0.60$, 0.68, 0.74, 0.82 Gyr. Following these time steps (Fig. 4) we confirm that the obvious drift of the magnetic field structures occurs in the outer part of the disk (between $r = 4.7$ kpc and $r = 6.8$ kpc). Namely, initially ($t = 0.60$ Gyr) magnetic and gaseous arms possess similar pitch angles, which are on order of $\sim 10°$. However, at later time steps the magnetic arms move to the inter-arm region and significantly decrease their pitch angles. We also notice that as the simulation proceeds the magnetic ring which encircles the bar (between $r = 3.2$ kpc and $r = 4.7$ kpc) becomes more and more waved. The additional dotted and dash-dotted lines presented in Fig. 4 are the co-rotation radius and the two Lindblad resonances: CR = 6.90 kpc, oILR = 3.06 kpc, OLR = 10.44 kpc (see Table 2).

4. Dependence on the bar angular velocity

The angular speed of any rotating pattern plays a crucial role in the dynamical behaviour of the gas in the galaxy. We computed our models with five different values of the bar angular speed $\Omega_{\rm bar}$ to check its influence upon the magnetic field structure. In all cases the angular speed of the bar is constant during the simulation. The rest of input parameters have the same values in all these models (see Tables 1 and 2).

4.1. The dynamical response of the gas

The value of the angular velocity of the bar plays an important role in the existance and appearance of the structures and patterns evolving in the galactic disk. In Fig. 5 we present the gas density distribution, velocity field, and simulated polarization maps in the galaxy for five different angular velocities of the bar, taken in the same time step. For lower values of the angular velocity of the bar, the corotation radius increases. Because of that, a very weak spiral pattern is visible for $\Omega_{\rm bar} = 15$ Gyr^{-1} ($r_{\rm CR} = 11.39$ kpc, OLR far beyond the computational domain, see Table 2). The existence of the bar is only marked by the arc-like structures inside the galactic disk. The enhancement of the gas density in this region fits the space between the two inner Lindblad resonances (calculated for the initial curve of rotation) iILR = 0.24 kpc and oILR = 4.64 kpc.

For the case of $\Omega_{\rm bar} = 20$ Gyr^{-1} ($r_{\rm CR} = 8.29$ kpc, $r_{\rm OLR} = 12.58$ kpc) the bar itself is well visible but still the corotation radius is too far for the spiral pattern to appear. In this case two inner Lindblad resonances exists. That causes strong enhancement of the gas density in the space between the iILR = 0.29 kpc and oILR = 3.73 kpc, forming an oval-shaped structure with no gas inside it.

Very well developed spiral arms in the disk are visible in the cases of $\Omega_{\rm bar} = 25$ Gyr^{-1} ($r_{\rm CR} = 6.90$ kpc, $r_{\rm OLR} = 10.44$ kpc) and $\Omega_{\rm bar} = 30$ Gyr^{-1} ($r_{\rm CR} = 5.94$ kpc, $r_{\rm OLR} = 8.91$ kpc).

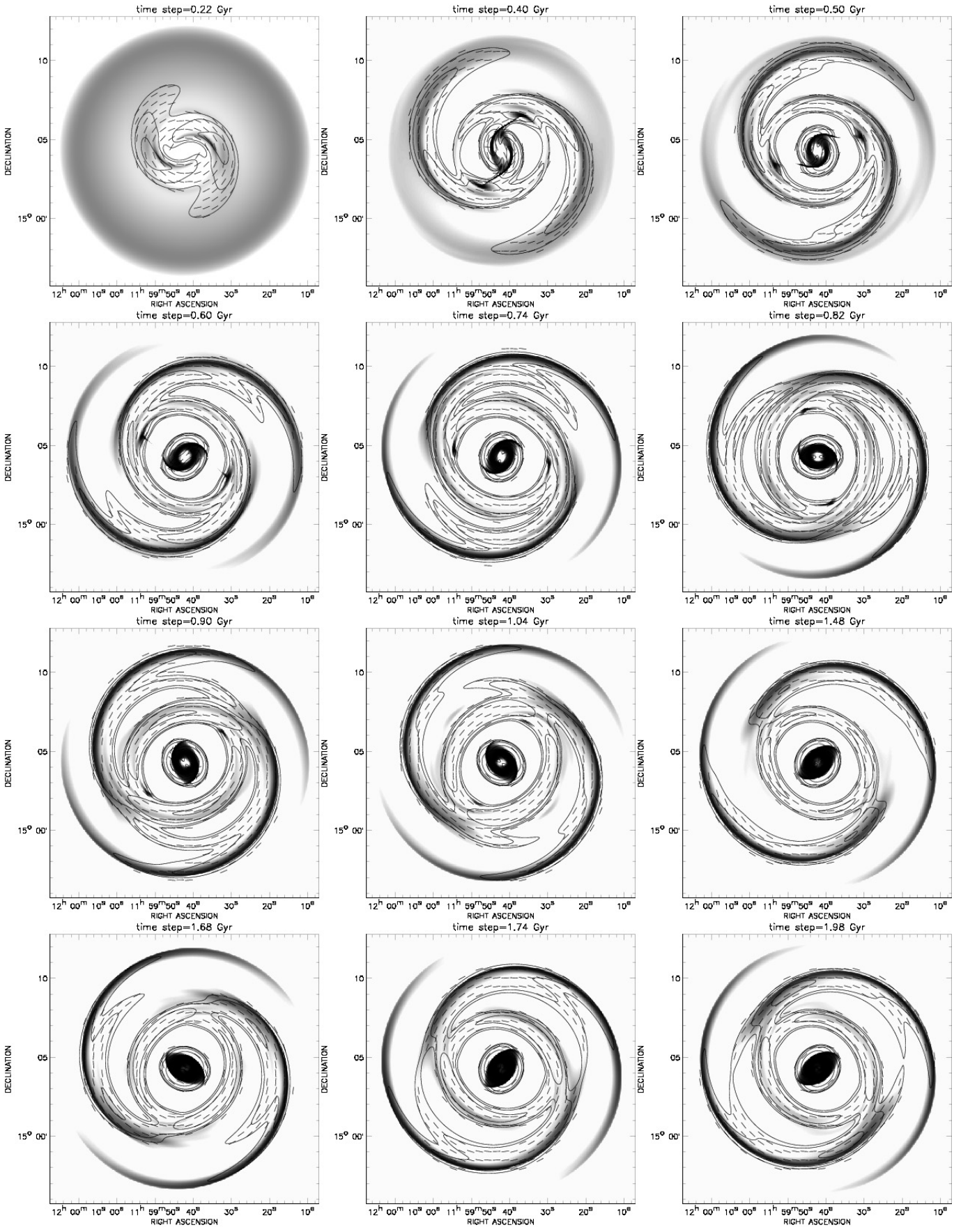

Fig. 3. Face-on polarization maps for selected times steps for model *omb25cs07*. Polarized intensity (contours) and polarization angles (dashes) are superimposed onto column density plots (grey-scale). All maps have been smoothed to the resolution 40″. The black color represents the regions with the highest density.

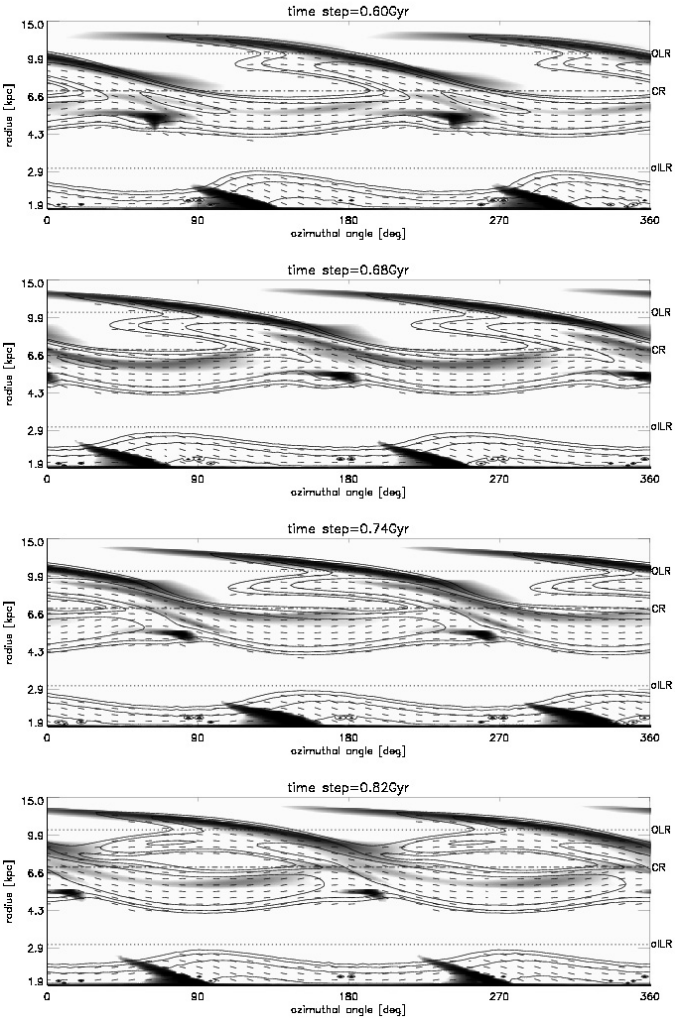

Fig. 4. Polarized intensity (contours) and polarization angles (dashes) for model *omb25cs07* superimposed onto the gas density (grey-scale, integrated along the line of sight) shown in the azimuth-log(r) frame at selected time steps. The co-rotation radius and two of the Lindblad resonances are shown as dash-dotted line and dotted line respectively.

However, iILR and oILR are getting closer to each other, so the central gas density enhancement forms a compact, oval-shaped structure with uniform gas density distribution inside.

For an extremely high angular velocity of the bar ($\Omega_{\rm bar}$ = 50 Gyr^{-1}, $r_{\rm CR}$ = 3.93 kpc, $r_{\rm OLR}$ = 5.81 kpc), where both corotation and OLR are situated inside the bar, the spiral arms are tightly wound around the center and the gas in the outer disk seems to be not undisturbed. Both inner Lindblad resonances are situated very close to the galactic center (iILR = 0.69 kpc, oILR = 1.31 kpc).

4.2. Influence of bar angular velocity on the magnetic field distribution

In this section we present the influence of the bar angular velocity on the magnetic field structure. Figure 6 shows the magnetic field evolution or the lowest value of the bar angular velocity, model *omb15cs07*. At the first time step (t = 0.67 Gyr) we obtain the inner magnetic structure, which corresponds to the central bar. At the end of the bar we also see small magnetic arms. Larger magnetic arms, which follow the gas distribution, are present in the outer part of the disk. As the simulation proceeds (time steps: t = 1.00 Gyr, t = 1.60 Gyr), the inner magnetic arms are more extended and the outer magnetic arms are located further from the center of the galaxy, slightly inclined to the dense gaseous ring (which indicates the co-rotation radius for the initial rotation curve). No drift of magnetic arms into the inter-arm region is observed.

The structure of the magnetic field that most resambles the reference model described in Sect. 3.2 we get for models *omb20cs07* (Fig. 7) and *omb30cs07* (Fig. 8). For both cases we initially obtained the same magnetic structures as in model *omb25cs07*. In both models we also see the drift of magnetic arms into the inter-arm region. Furthermore, the magnetic arms starts to detach from the gaseous spiral approximately at the same time ($t \sim$ 50 Gyr). However, the time at which magnetic arms connect with the magnetic ring and form the double-ring structure is different for all models. This distinction is caused by the bar angular velocity, which determines the distance between corotation radius and OLR ($R_{\rm OLR-CR}$). Namely, for higher values of the bar angular velocity we get lower values of the $R_{\rm OLR-CR}$. Thus for $\Omega_{\rm bar}$ = 30.0 Gyr^{-1} ($R_{\rm OLR-CR}$ = 2.97 kpc) the magnetic arms connect with the magnetic ring faster than for $\Omega_{\rm bar}$ = 20.0 Gyr^{-1} ($R_{\rm OLR-CR}$ = 4.29 kpc). For the model *omb30cs07* (Fig. 8) the magnetic arms detach from the central ring at a time t = 0.92 Gyr and are unable to drift again into the inter-arm region. Central enhancements of the density and polarization fit the space inside the oILR, the inner magnetic ring extends to the co-rotation radius and the connection between the inner magnetic ring and outer magnetic arms lies exactly at the distance equal to the OLR. Both the gaseous and magnetic arms extend beyond the OLR. For the model *omb20cs07* (Fig. 7) the magnetic arms are connected with the inner magnetic ring until the end of the simulations (t = 2.00 Gyr). The central density and polarization enhancements are situated exactly inside the oILR, the inner magnetic ring lies inside the co-rotation radius and the outer magnetic arms extend to the OLR.

For the highest value of the bar angular velocity (model *omb50cs07*, Fig. 9) the magnetic field maxima follow the gas distribution for the whole simulation time. Thus, the magnetic arms do not detach from the gaseous ones, but form with them a ring which encircles the bar. The ring is located beyond the OLR.

To demonstrate the influence of the bar angular velocity on the magnetic filed distribution we show the simulated polarization maps for all models taken at the same time (Fig. 5, right column). The obvious distinction is visible even for the very similar values of the bar angular velocity ($\Omega_{\rm bar}$ = 20.0 Gyr^{-1}, $\Omega_{\rm bar}$ = 25.0 Gyr^{-1}, $\Omega_{\rm bar}$ = 30.0 Gyr^{-1}). This confirms that the value of the bar angular velocity is crucial not only for the gas disrtibution but also for the magnetic field evolution.

5. Influence of the sound speed

Patsis & Athanassoula (2000) investigated the influence of the sound speed upon the gas distribution in their models and showed that it is an important parameter for the gas dynamics in the inner part of the bar and the bar morphological structure. Inspired by this result, we performed calculations of new models, changing the value of the sound speed $c_{\rm s}$ in the range between 5 km s^{-1} and 10 km s^{-1}. We did not find any significant differences between the appearance of structures, gas dynamics or the magnetic field configuration in these models (see Fig. 10). Of course both the construction of the numerical model (basic assumptions about initial gas distribution and the sound speed

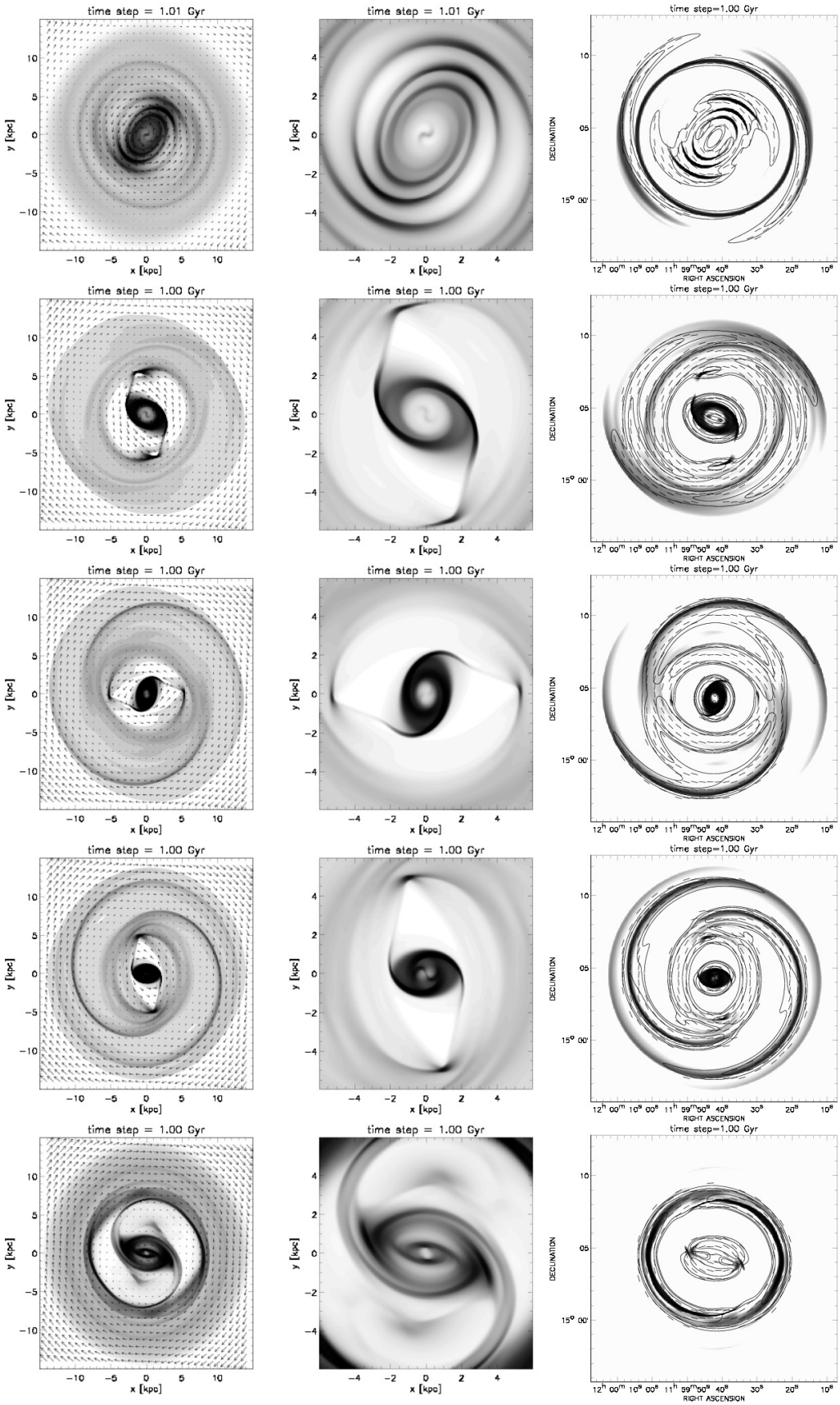

Fig. 5. Angular velocity influence on the gas dynamics and magnetic field structure: $\Omega_{\rm bar} = 15.0$ Gyr^{-1} in 1st row, $\Omega_{\rm bar} = 20.0$ Gyr^{-1} in 2nd row, $\Omega_{\rm bar} = 25.0$ Gyr^{-1} in 3rd row, $\Omega_{\rm bar} = 30.0$ Gyr^{-1} in 4th row, $\Omega_{\rm bar} = 50.0$ Gyr^{-1} in 5th row. *Left column*: velocity field in the frame rotating with the bar (vectors) and the gas density distribution in the galactic mid-plane (grey-scale, darker means greater density). *Middle column*: column density (darker means higher column density) for the inner 6 kpc × 6 kpc part of galaxy. *Right column*: polarized intensity (contours), polarization angles (dashes) and column density (grey-scale) smoothed to the resolution 40″.

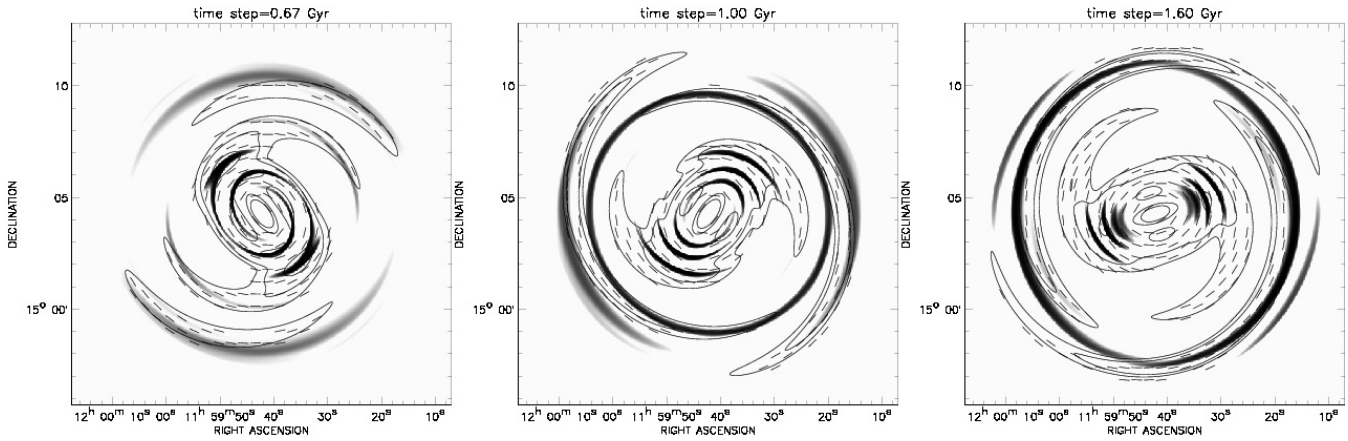

Fig. 6. Face-on polarization maps at selected times steps for model *omb15cs07*: polarized intensity (contours), polarization angle (dashes) and column density (grey-scale). All maps have been smoothed to the resolution 40″. The black color represents the regions with the highest density.

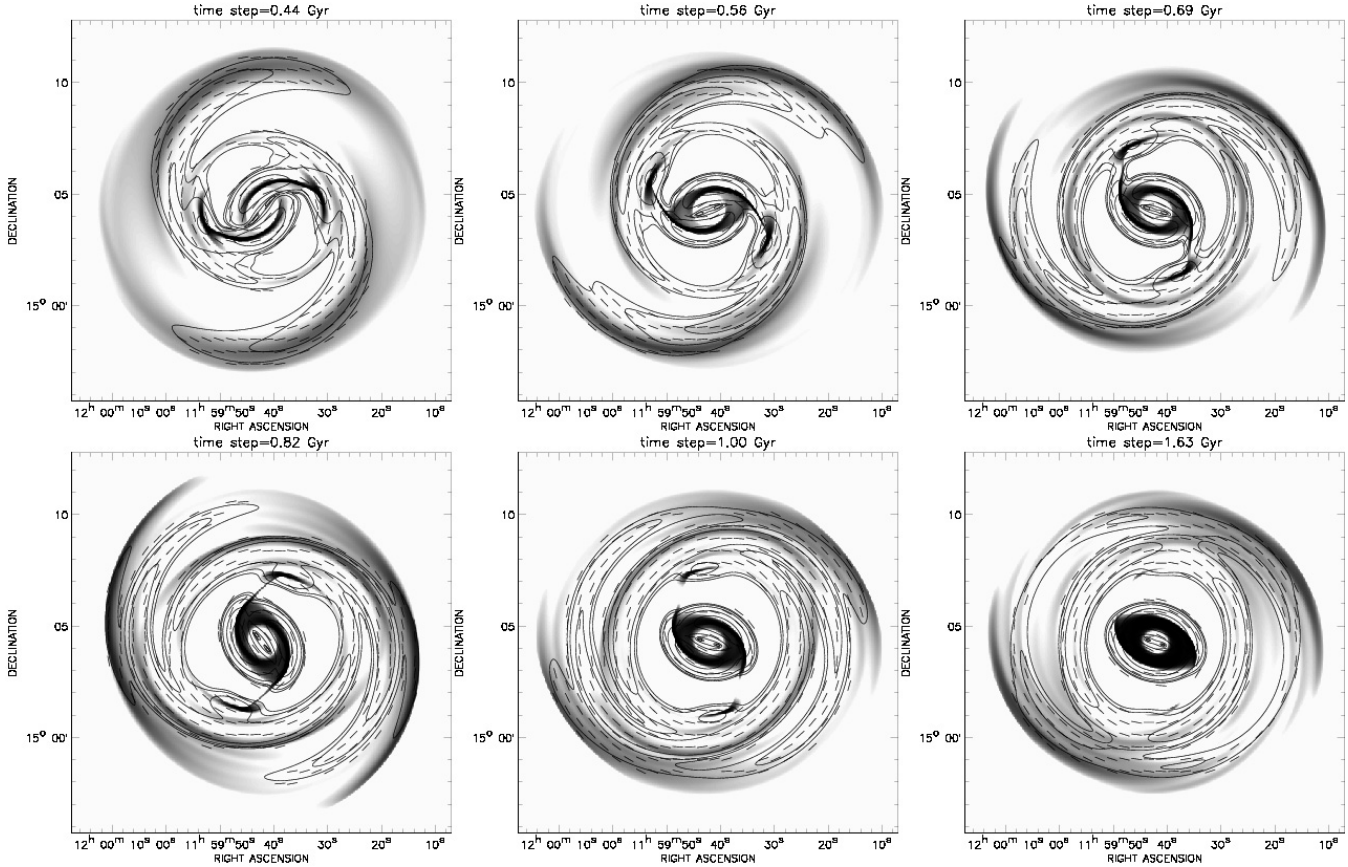

Fig. 7. Face-on polarization maps at selected times steps for model *omb20cs07*: polarized intensity (contours), polarization angle (dashes) and column density (grey-scale). All maps have been smoothed to the resolution 40″. The black color represents the regions with the highest density.

values) and the numerical methods used here and in Patsis & Athanassoula (2000) were different and a simple comparison of results is not possible.

6. Discussion

6.1. Gas dynamics in the context of earlier experiments

Although the most important aim of these numerical experiments was to investigate the relation of the observed magnetic field structures to the dynamical ones, the agreement with the earlier, dynamical studies of this problem is also important. In Sect. 3 we show that the basic dynamical features of our barred galaxies are very similar to those constructed by Athanassoula (1992). Introducing the bar potential into the unperturbed disk galaxy, we obtained characteristic structures, such as shocks identified with dust lanes along the leading edges of the bar and spiral arms propagating in the outer parts of the galactic disk outside the bar. Moreover, in Sect. 4 we showed that there is an obvious relation between the bar angular velocity and the existence as well as the shapes of these structures: lower values of $\Omega_{\rm bar}$ (related with higher values of Lagrangian radius in Athanassoula 1992) generate straight or slightly curved dust lanes and an elliptical bulge, while higher values of the bar angular velocity

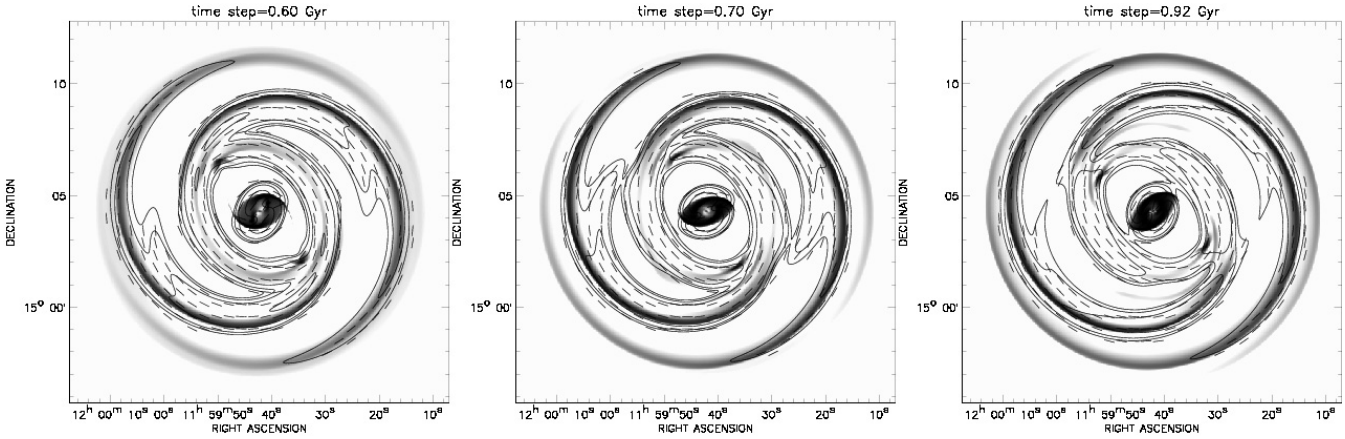

Fig. 8. Face-on polarization maps at selected times steps for model *omb30cs07*: polarized intensity (contours), polarization angle (dashes) and column density (grey-scale). All maps have been smoothed to the resolution 40″. The black color represents the regions with the highest density.

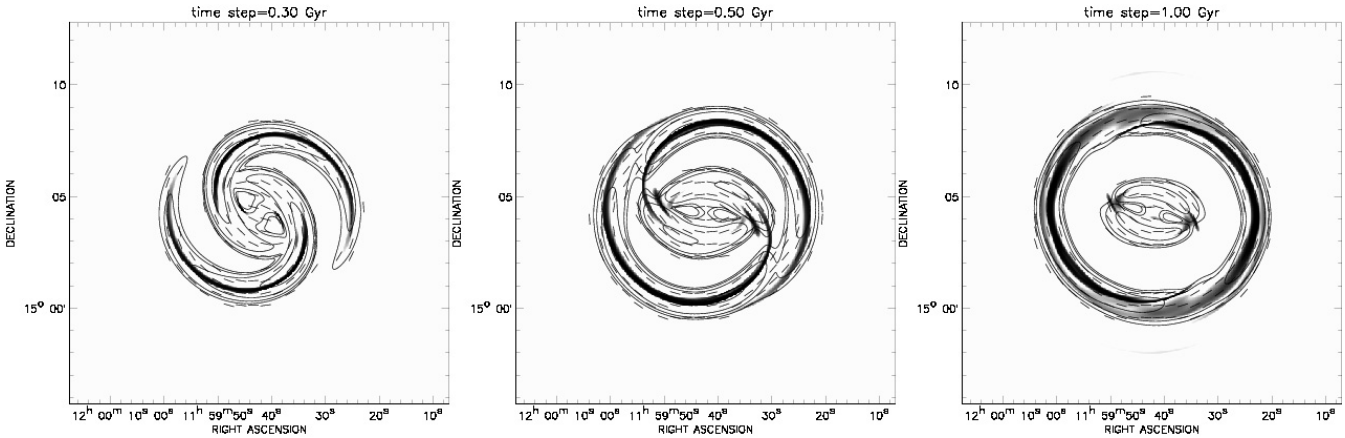

Fig. 9. Face-on polarization maps at selected times steps for model *omb50cs07*: polarized intensity (contours), polarization angle (dashes) and column density (grey-scale). All maps have been smoothed to the resolution 40″. The black color represents the regions with the highest density.

(shorter Lagrangian radius) are responsible for extremely curved dust lanes and boxy/peanut bulges. Unfortunately the sound speed analysis gave different results, but some suggestions for further work can be formulated. Patsis & Athanassoula (2000) showed that sound speed of the gas also may affect the structures observed in barred galaxies. For extremly high values of the sound speed (not necessarily realistic) they obtained very elongated bars, almost needle-shaped. But for sound speeds in the range of 10 to 15 km s^{-1} the differences in the bar shapes are very small, and their structures are similar for those obtained in our experiments for the sound speeds in the range of 5 to 10 km s^{-1}.

6.2. Relation to other works on magnetic field evolution in barred galaxies

As described above the value of the bar angular velocity determines the gas density distribution. From observations (Chyży et al. 2007) and numerical simulations (Kotarba et al. 2009) we know that the magnetic field typically follows a nearby spiral density wave. Thus it is not surprising that the magnetic field configuration in our simulations depends on the bar angular velocity.

Several researchers have numerically approached the problem of the magnetic field evolution in barred galaxies (Moss et al. 1998, 1999; Otmianowska-Mazur et al. 1997; Moss et al. 2001, 2007) to analyze the role of a mean-field dynamo theory in generation and maintenance of the large-scale magnetic field in barred galaxies. In their simulations they reproduced many of the observed features of barred galaxies, e.g. magnetic arms aligned along the gaseous ones, magnetic field in the inter-arm regions or magnetic field pattern along the dust lanes in a bar. However, they did not find the mechanism which is responsible for shifting of the magnetic arms from the gasoues ones to the inter-arm space. As we mentioned in the intorduction, the concept of the magnetic field drift into the inter-arm region was described earlier only in two papers (Otmianowska-Mazur et al. 2002; Kulesza-Żydzik et al. 2009). In the aforesaid paper the authours found this mechanism for the first time, but in those calculation they did not take into account the back-reaction of magnetic field to the gas, which could be crucial in these studies. The second paper mentioned showed that the process responsible for the shifting of the magnetic arms into the inter-arm space worked. Compared to the present paper, two of our earlier mentioned papers lacked a detailed study of the influence of the bar angular velocities on the magnetic field configurations. Indeed, the bar angular velocity is crucial for the formation of gaseous and magnetic arms. For particular values of the bar angular velocity ($\Omega_{\rm bar}$ = 25.0 Gyr^{-1}, $\Omega_{\rm bar}$ = 30.0 Gyr^{-1}) we obtained the magnetic arms drifting into the inter-arm region. For the rest of models the shifting of the magnetic arms is much more difficult.

The calculated synthetic polarization maps can be directly compared with the observation of barred galaxies. Our

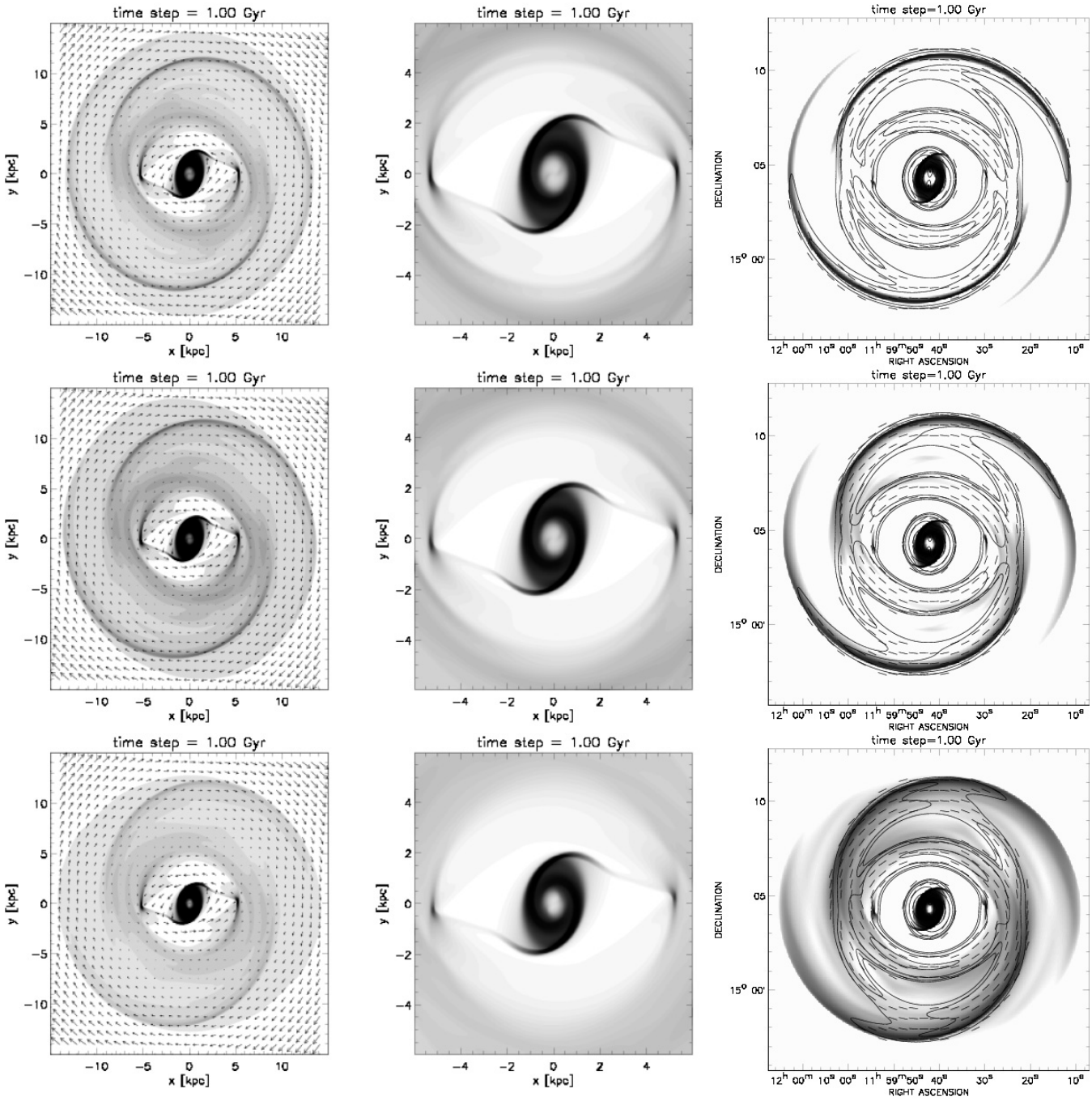

Fig. 10. *Left column*: gas density distribution (grey-plot) and velocity field in the rotating bar frame (vectors) in the galactic midplane. *Middle column*: column density of the gas (grey-scale) in the inner 6 kpc × 6 kpc region. *Right column*: polarized intensity (contours), polarization angles (dashes) and gas column density (grey-scale). Three different values of the sound speed are $c_s = 5$ km s^{-1} (1st row), $c_s = 7$ km s^{-1} (2nd row) and $c_s = 10$ km s^{-1} (3rd row). All polarization maps have been normalized to their initial distribution and smoothed to the resolution 40″.

simulations bears some resemblance to observations of barred galaxies shown by Beck et al. (2002). The galaxy NGC 1365 exhibits inter-arm areas filled with polarized emission. In this case even the maxima of polarized intensity are located between arms. The magnetic field orientation corresponds to the spiral arm direction. A similar situation is shown in two other galaxies: NGC 7479, and NGC 1672, but in the latter case the asymmetry reduces the similarity.

Note that without taking into account the dynamo action we are able to get realistic models of the magnetic field structures. The most important are the magnetic arms, which are detached from the gaseous spiral. However, in order to find higher and more realistic values of the magnetic pitch angles than those obtained in this paper, we are going to include the cosmic-ray dynamo mechanism in our next simulations.

7. Conclusions

We have examined the results of 3D simulations of the magnetic field evolution in spiral barred galaxies. Our findings may be summarized as follows:

– The results of our experiments agree with the earlier ones, especially the dynamical behaviour of the gas (see

Athanassoula 1992) and the magnetic field general structure (see Otmianowska-Mazur et al. 2002; Kulesza-Żydzik et al. 2009). The not visible relation between the sound speed value and the morphological structure of the bar observed by Patsis & Athanassoula (2000) may be the effect of the differences between the considered models of barred galaxies. However, the dependence of the spiral arms existence on the bar angular velocity value can be discussed also in the context of the magnetic field structures: the drift of the magnetic field to the inter-arm regins is well visible only for some values of the bar angular speed.

– The synthetic polarization maps obtained in our experiments bears some resemblance to the observed ones in the context of the general properties of the magnetic field structures in bar galaxies.

Acknowledgements. This work was supported by the Polish Ministry of Science and Higher Education through grants: 92/N-ASTROSIM/2008/0 and 3033/B/H03/2008/35. The computations presented here have been performed on the GALERA supercomputer in TASK Academic Computer Centre in Gdańsk.

References

Athanassoula, E. 1992, MNRAS, 259, 345
Athanassoula, E. 2005a, MNRAS, 358, 1477
Athanassoula, E. 2005b, Cel. Mech. Dyn. Astron., 91, 9
Athanassoula, E. 2009, [arXiv:0910.5180v1]
Beck, R., Ehle, M., Shoutenkov, V., et al. 1999, Nature, 397, 324
Beck, R., Shoutenkov, V., Ehle, M., et al. 2002, A&A, 391, 83
Beck, R., Beck, R., Fletcher, A., et al. 2005, A&A, 444, 739
Binney, J., & Tremaine, S. 2008, Galactic Dynamics, second edn. (Princeton University Press)
Chyży, K. T., Ehle, M., & Beck, R. 2007, A&A, 474, 415
Del Zanna, L., Bucciantini, N., & Londrillo, P. 2003, A&A, 400, 397
Englmaier, P., & Gerhard, O. 1997, MNRAS, 287, 57
Eskridge, P., Frogel, J., Pogge, R., et al. 2002, ApJS, 143, 73E
Evans, C. R., & Hawley, J. F. 1988, ApJ, 332, 659
Ferrers, N. M. 1877, Quart. J. Pure Appl. Math., 14, 1
Grosbol, P., Pompei, E., & Patsis, P. A. 2002, ASPC, 275, 305G
Harnett, J., Ehle, M., Fletcher, A., et al. 2004, A&A, 421, 571
Kotarba, H., Lesch, H., Dolag, K., et al. 2009, MNRAS, 397, 733
Kowal, G., Lazarian, A., Vishniac, E. T., & Otmianowska-Mazur, K. 2009, ApJ, 700, 63
Kulesza-Żydzik, B., Kulpa-Dybeł, K., Otmianowska-Mazur, K., Kowal, G., & Soida, M. 2009, A&A, 498, L21
Moss, D., Korpi, M., Rautiainen, P., & Salo, H. 1998, A&A, 329, 895
Moss, D., Rautiainen, P., & Salo, H. 1999, MNRAS, 303, 125
Moss, D., Shukurov, A., Sokoloff, D., Beck, R., & Fletcher, A. 2001, A&A, 380, 55
Moss, D., Snodin, A., Englmaier, P., et al. 2007, A&A, 465, 157
Otmianowska-Mazur, K., & Chiba, M. 1995, A&A, 301, 41
Otmianowska-Mazur, K., von Linden, S., Lesch, H., & Skupniewicz, G. 1997, A&A, 323, 56
Otmianowska-Mazur, K., Elstner, D., Soida, M., & Urbanik, M. 2002, A&A, 384, 48
Patsis, P. A., & Athanassoula, E. 2000, A&A, 358, 45